Classification of the global Sentinel-1 SAR vignettes for ocean surface process studies

Chen Wang, Pierre Tandeo, Alexis Mouche, Justin Stopa, Victor Gressani, Nicolas Longépé, Douglas Vandemark, Ralph Foster, Bertrand Chapron

Classification of the global Sentinel-1 SAR vignettes for ocean surface process studies

Chen Wang[a,b,*], Pierre Tandeo[b], Alexis Mouche[a], Justin E. Stopa[c], Victor Gressani[a], Nicolas Longepe[d], Douglas Vandemark[e], Ralph C. Foster[f], Bertrand Chapron[a]

[a]*IFREMER, Univ. Brest, CNRS, IRD, Laboratoire d'Oceanographie Physique et Spatiale (LOPS), Brest, France*
[b]*IMT Atlantique, Lab-STICC, UBL, Brest, France*
[c]*Department of Ocean Resources and Engineering, University of Hawaii at Manoa, Hawaii, USA*
[d]*Space and Ground Segment, Collecte Localisation Satellites (CLS), Plouzane, France*
[e]*Ocean Processes Analysis Laboratory, University of New Hampshire, New Hampshire, USA*
[f]*Applied Physics Laboratory, University of Washington, Seattle, USA*

Abstract

Spaceborne synthetic aperture radar (SAR) can provide finely-resolved (meters-scale) images of ocean surface roughness day-or-night in nearly all weather conditions. This makes it a unique asset for many geophysical applications. Initially designed for the measurement of directional ocean wave spectra, Sentinel-1 SAR wave mode (WV) vignettes are small 20 km scenes that have been collected globally since 2014. Recent WV data exploration reveals that many important oceanic and atmospheric phenomena are also well captured, but not yet employed by the scientific community. However, expanding applications of this whole massive dataset beyond ocean waves requires a strategy to automatically identify these geophysical phenomena. In this study, we propose to apply the emerging deep learning approach in ocean SAR scenes classification. The training is performed using a hand-curated dataset that describes ten commonly-occurring atmospheric or oceanic processes. Our model evaluation relies on an independent assessment dataset and shows satisfactory and robust classification results. To further illustrate the model performance, regional patterns of rain and sea ice are qualitatively analyzed and found to be very consistent with independent remote sensing datasets. In addition, these high-resolution WV SAR data can resolve fine, sub-km scale, spatial structure of rain events and sea ice that complement other satellite measurements. Overall, such automated SAR vignettes classification may open paths for broader geophysical application of maritime Sentinel-1 acquisitions.

Keywords: Synthetic aperture radar (SAR), Ocean surface phenomena, Sentinel-1 wave mode, Deep learning, Convolutional neural network (CNN), Image classification

1. Introduction

The spaceborne synthetic aperture radar (SAR) is a well-established technique to collect high-resolution sea surface backscatter data during day and night in most weather conditions. Over the ocean, SAR images provide an estimate of the sea surface roughness primarily through backscattering of short waves (Alpers et al., 1981; Hasselmann et al., 1985; Hasselmann and Hasselmann, 1991), where this small-scale (cm) roughness responds to the near-surface ocean winds (Lehner et al., 2000; Winstead et al., 2006; Mouche et al., 2012). In addition, these short waves are also modulated by ocean swell (Heimbach et al., 1998; Lehner et al., 2000; Collard et al., 2009), upper ocean processes (Johannessen et al., 1996; Rascle et al., 2017; Jia et al., 2018), and atmospheric phenomena (Alpers and Brümmer, 1994; Young et al., 2005; Winstead et al., 2006; Li et al., 2007, 2013; Alpers et al., 2016). Beginning with SEASAT in 1978, ocean SAR imagery has been widely used to examine numerous air-sea interaction processes (Meadows et al., 1983; Gerling T W, 1986; Carsey and Holt, 1987; Fu and Holt, 1982; Katsaros and Brown, 1991). Since then, ever-improving SAR data have been obtained by satellite missions that include ERS-1/2, Envisat/ASAR, RADARSAT-1/2, TerraSAR-X, TanDEM-X and Sentinel-1 constellation.

However, global-scale applications of ocean SAR data remain quite limited. This is largely because the wide swath SAR images are not routinely collected over the open ocean. These acquisitions mainly focus on land, Arctic regions, and near the coasts. Thus, most previous ocean SAR data investigations only involve limited regional or single SAR scene case study (Alpers and Brümmer, 1994; Babin et al., 2003; Sikora et al., 2011; Li et al., 2013; Alpers et al., 2016). One exception is the wave mode (WV) dedicated to retrieving ocean wave proprieties at global scale (Kerbaol et al., 1998; Stopa et al., 2016). The WV has been developed for ERS-1/2 (1991-2003) and Envisat/ASAR (2002-2012), and now introduced to Sentinel-1 (2014-present) and Gaofen-3 (2016-present). It normally collects relative small SAR images (typically 5 to 10 km square) along the orbit with a distance of about 100 km in between. This is sufficient for ocean wave spectrum retrieval and empirically estimation of the total significant wave height (Heimbach et al., 1998; Collard et al., 2009; Stopa and Mouche, 2017), which can be used in wave forecasting. At present, the routine WV measurements are only available from the Sentinel-1 (S-1) A&B (Torres et al., 2012). It was improved upon Envisat and ERS by having finer spatial resolution (4 m), higher signal-to-noise (which reduces speckle noise), larger scene footprint (20 by 20 km), and increased global sampling.

*Corresponding author
Email address: Chen.Wang@ifremer.fr (Chen Wang)

Wang et al. (2019) demonstrated that the S-1 WV dataset has the potential for new studies on air-sea interactions at scales of 0.5-10 km. The primary advantage of the S-1 WV dataset is its ability of measuring high resolution sea surface roughness globally (~120k images per month). However, without an automated means to identify the geophysical features captured by each image, the potential would remain untapped. For example, previous studies have relied solely on visual inspection to identify SAR images with wind streaks before performing statistical analysis or surface wind direction derivation (Lehner et al., 2000; Levy, 2001; Mouche et al., 2012; Zhao et al., 2016). Such manual classification approach is impractical for the huge volume of S-1 WV data. Similarly, dedicated classic machine learning algorithms have mostly been developed for specific applications such as detection of oil spills and ships. These methods depend on the empirically hand-crafted features, which are usually insufficient to generalize the local variations, shapes and structural patterns of different geophysical phenomena (Topouzelis and Kitsiou, 2015; Zhang et al., 2016).

This study attempts to train a deep convolutional neural network (CNN) to classify the ten prescribed geophysical phenomena seen in WV vignettes. Deep CNN models have been applied with great success in detection, segmentation, and recognition of objects, features, and textures within digital images (LeCun et al., 2015). They have also been applied to hyperspectral and optical remote sensing imagery (Zhao and Du, 2016; Li et al., 2017; Hu et al., 2015; Cheng and Han, 2016; Zhou et al., 2017). However, the primary use of CNN in ocean SAR application has mostly been for target recognition (Zhang et al., 2016; Zhu et al., 2017). In general, CNN is a multilayer architecture that can be trained to automatically extract the optimal image features and to amplify distinctions between images (LeCun et al., 2015; Zhang et al., 2016). A practical and effective way to develop a robust CNN for a specific application is to re-train an existing image recognition model. This so-called transfer-learning or fine-tuning strategy has been proven to be more efficient and practical than creating and training a new CNN architecture from scratch (Yosinski et al., 2014; Zhu et al., 2017; Cheng et al., 2017; Too et al., 2018; Wang et al., 2018a).

In this paper, we adapt the Inception-v3 CNN (Szegedy et al., 2015) to train a model dedicated to the classification of S-1 WV vignettes, called CMwv. The involved datasets are described in section 2. Section 3 demonstrates the training process of CMwv and illustrates the model performance based on an independent assessment dataset. In section 4, we compare our classification results qualitatively with rain precipitation from Global Precipitation Measurement (GPM) and sea-ice concentration from Special Sensor Microwave Imager (SSM/I). Conclusions follow in section 5.

2. Datasets

This study uses ocean SAR vignettes from S-1 WV, precipitation data from GPM and sea ice concentration data from SSM/I. To train the CNN architecture, we create training datasets drawn from the labelled TenGeoP-SARwv database (Wang et al., 2018b). In addition, to assess and quantify the performance of CMwv, we build an assessment dataset of 10,000 visually verified images. All datasets are described in the following.

2.1. S-1 WV

The S-1 mission is a constellation of two (A&B) polar-orbiting, sun-synchronous SAR satellites (Torres et al., 2012). They were launched by European Space Agency (ESA) in April of 2014 and 2016, respectively. The two satellites share the same orbital plane, which crosses the equator at approximately 0600 or 1800 local time, with a 180° phase difference to provide an effective 6-day repeat cycle. The S-1 microwave SAR instruments have a 5.5 cm wavelength (C-band). WV is the default mode over the open ocean unless other imaging mode collections are requested. According to the defined Mission Operation Scenario, there is no WV acquisition in the Arctic Ocean, closed seas (Red, Black, Mediterranean and Caribbean seas) and coastal areas. Figure 1 displays the spatial coverage of S-1A WV data acquired in July of 2016. Although only S-1A WV data is used in this study, S-1B images have essentially equivalent characteristics with S-1A. Thus, the combination of S-1A and S-1B will expand sampling in time and space for different geophysical phenomena applications. Moreover, the developed classification model and results presented hereafter are also applicable to S-1B.

S-1 WV vignettes are acquired in a 'leapfrog' pattern at two alternating center incidence angles of 23° (WV1) and 36.5° (WV2) every 100 km along the flight track. Each vignette has a 20 by 20 km footprint with 5 m spatial resolution. The default radar polarization is VV, though some HH images have been acquired. Combining both satellites and WV incidence angles, approximately 120,000 vignettes per month are acquired. This study focuses on the VV polarized SAR vignettes as they comprise more than 99% of acquisitions to date. Also, data quality control is carried out by removing data files with the following criteria:

- **HH polarization:** HH-polarized images are excluded.
- **Land contamination:** The distance of one vignette center (longitude and latitude) to the nearest coastline is calculated based on the dataset of Distance from Nearest Coastline

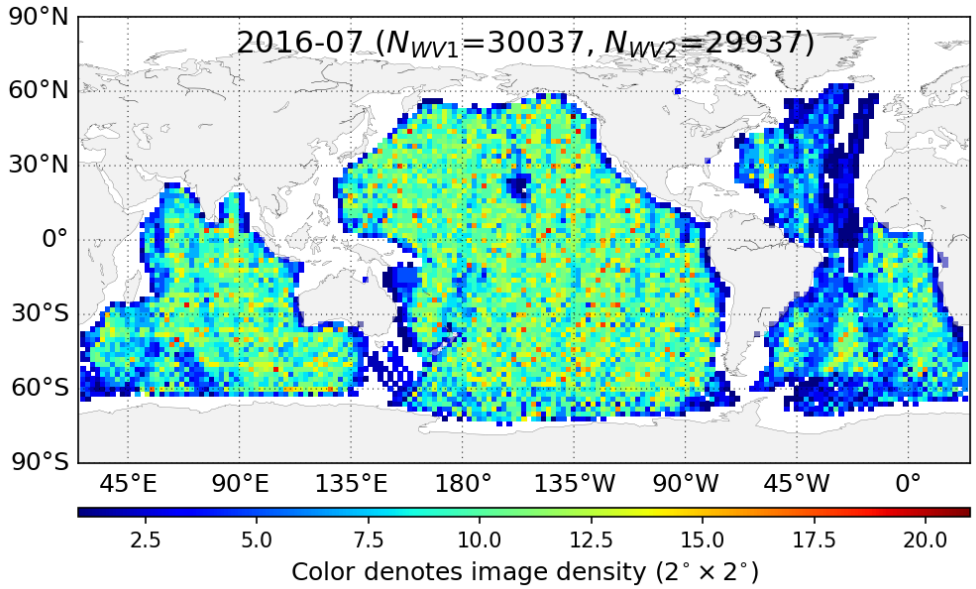

Figure 1: Global distribution of the WV SAR data obtained by S-1A in July of 2016. Color is indicative of the SAR image density in 2° by 2° spatial grid.

(DNC[1]). We filter out the vignettes if their center is over the land.

- **Low mean signal intensity:** We filter out the low-quality vignettes by limiting the mean Normalized Radar Cross Section (NRCS) to be larger than -22 dB, which is the Noise Equivalent Sigma Zero (Torres et al., 2012).

2.2. *TenGeoP-SARwv dataset*

TenGeoP-SARwv is a labelled dataset of more than 37k ocean SAR images corresponding to ten commonly-observed and expertly-defined geophysical phenomena (Wang et al., 2019). These ten choices, though somewhat subjective, were selected and defined after an extensive review of the S-1 WV data and with reference to past ocean SAR studies. This study denotes the classes as pure ocean waves (PureWave), wind streaks (WindStreak), micro-convective cells (WindCell), rain cells (RainCell), biological slicks (BioSlick), sea ice (SeaIce), icebergs (IceBerg), low wind areas (LowWind), atmospheric fronts (AtmFront), and oceanic fronts (OcnFront). Thousands of VV-polarized vignettes for each case were manually selected from the S-1A WV acquisitions in 2016. These vignettes are chosen with the criteria that within one scene, one geophysical

[1]The Distance from Nearest Coastline dataset is available at http://oos.soest.hawaii.edu/erddap/info/dist2coast_1deg/index.html

phenomenon dominates with its specific signature or pattern. It is worth noticing that PureWave signatures normally exist in SAR images as background for other classes. Example vignettes of the ten defined classes are displayed in Figure 2. These visually-identified and tagged SAR scenes, 37560 in total, are provided in formats of Portable Network Graphics (PNG) and Georeferenced Tagged Image File Format (GeoTIFF). Despite the fact that the GeoTIFF product maintains high precision of the original data, PNG files are more suitable for visual interpretation and satisfy the training input requirement for CNN models. Thus, PNG product is the dataset of interest in this study. It is important to note that the detectability of SAR on these phenomena, especially these modulations induced by the surface wind, can differ for WV1 versus WV2. Because the complex response of C-band radar scatter of the sea surface depends primarily on the incidence angle and the relative angle between the radar and the surface wind direction. Under some atmospheric conditions such as strong winds (>15 m/s), the backscatter is dominated by sea states (winds and waves). Consequently, other phenomena except ocean waves can not be well captured.

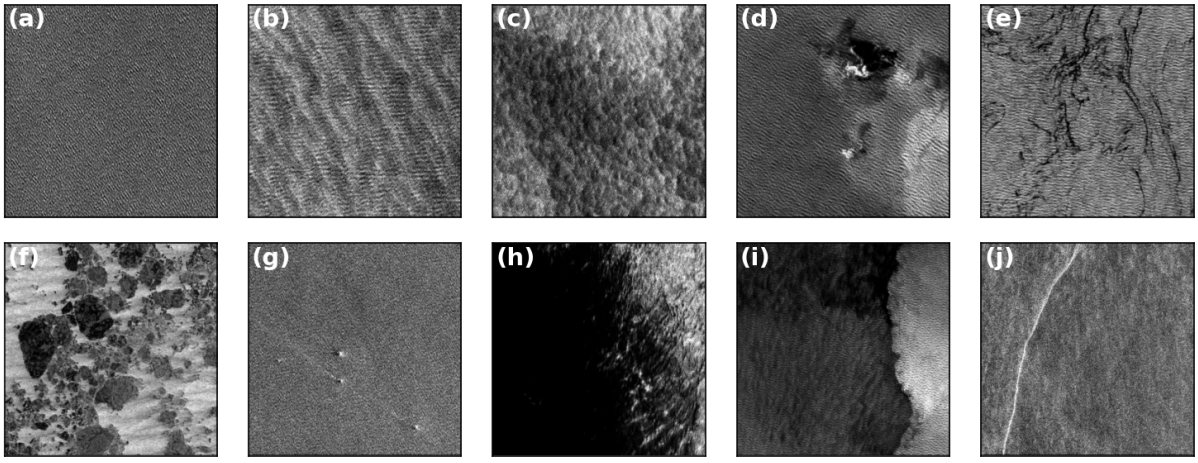

Figure 2: Ten vignette examples of expertly-defined geophysical phenomena. From (a) to (j) are pure ocean waves (PureWave), wind streaks (WindStreak), micro convective cells (WindCell), rain cells (RainCell), biological slicks (BioSlick), sea ice (SeaIce), icebergs (IceBerg), low wind area (LowWind), atmospheric front (AtmFront) and oceanic front (OcnFront).

2.3. Assessment dataset

S-1 WV SAR vignettes are able to capture a wide range of ocean surface geophysical processes and the most common ten categories have been included in the TenGeoP-SARwv. To assess and quantify performance of the developed classification model on the whole WV database, an independent assessment dataset is thus created. 5000 WV1 and WV2 vignettes respectively were

randomly selected from 2016 S-1A acquisitions and classified by visual inspection. A less strict criteria of PureWave was adopted to make this validation dataset representative of the actual WV measurements. We then apply the classification model to each of these scenes. The resulting class identifications were compared to visual results, which is a skill test commonly used in image classification modeling (Zhang et al., 2016; Cheng et al., 2017). For the vignettes that do not belong to any of the ten defined classes, we sort them into a special 'The Other' category (TheOther). These more infrequent phenomena include, but are not limited to, oceanic internal waves (Alpers and Huang, 2011; Jia et al., 2018), atmospheric gravity waves (Chunchuzov et al., 2000; Li et al., 2013), upwelling regions (Jackson et al., 2004), and irregular atmospheric patterns.

2.4. Rain precipitation from GPM and IMERG

The GPM mission is an international satellite network that provides global estimates of rainfall and snowfall from space (Hou et al., 2014). A primary instrument is the GPM Core Observatory that was launched in February 2014 by the National Aeronautics and Space Administration (NASA) and the Japan Aerospace and Exploration Agency (JAXA). This Core Observatory carries the first dual-frequency (Ku-/Ka-band) precipitation radar (DPR) and a multichannel microwave imager (GMI). The Ku-band radar accurately measures moderate to heavy rain rates and the Ka-band radar can measure light rain and snowfall. They provide cross-track swaths of 245 km (Ku) and 120 km (Ka) with 5 km resolution. Retrieved precipitation estimates from the swath measurements are available at the NASA data center (`https://pmm.nasa.gov/data-access/downloads/gpm`). In addition, the Integrated Multi-satellitE Retrievals for GPM (IMERG) is a gridded precipitation product that combines all satellite precipitation measurements. In this study, we collocate GPM level-2 (swath) DPR Ku-only surface rain precipitation data with S-1A WV vignettes acquired from March 2016 to February 2017. Spatial and temporal collocation criteria of 35 km and less than 10 mins are used and result in 2588 matched data pairs. The mean precipitation value for DPR measurements averaged across the 35 km square is used. We also use the IMERG 0.1°-monthly product to qualitatively validate the global and seasonal features of CMwv-classified rain events. Results and discussions are given in section 4.1.

2.5. Ice concentration from SSM/I

Sea ice concentration maps are produced by applying the Artist Sea Ice (ASI) algorithm to the brightness temperatures from Special Sensor Microwave Imager (SSM/I) radiometer (Ezraty et al., 2007). The concentration product has been operational since 1992 with 12.5 km spatial resolution. It is publicly available at `ftp://ftp.ifremer.fr/ifremer/cersat/products/`

gridded/psi-concentration/. The seasonal sea ice concentration is computed based on the daily data, and compared with the CMwv-classified sea ice event occurrences (see section 4.2).

3. Automated ocean SAR scene classification

This section describes how the automated classifier for S-1 WV ocean SAR vignettes was developed by re-training the Inception-v3 CNN. The performance of this tool is evaluated and quantified using the independent assessment dataset described in section 2.3.

3.1. Inception-v3 and training strategies

Many successful CNN architectures have shown solid performance in the ImageNet large-Scale Visual Recognition Challenge (ILSVRC) (Russakovsky et al., 2015). In this study, we use the Inception-v3 architecture proposed by Google in 2015 (Szegedy et al., 2015; Szegedy et al., 2016) to demonstrate the potential of deep CNN in identifying and classifying geophysical phenomena from ocean SAR scenes. The Inception model was firstly introduced as GoogLeNet or Inception-v1 (Szegedy et al., 2015), a classic deep CNN architecture. The initial Inception architecture was refined in many ways. A first improvement was introduced in the Inception-v2 of batch normalization to accelerate the training process (Szegedy et al., 2016). While later, the Inception-v3 used additional factorization ideas to augment the number of convolutions without increasing the computational cost. It achieves remarkable performance with 94.4% top-5 accuracy on the ILSVRC 2012 classification dataset. We choose Inception-v3 in this study because of its promising performance and easy implementation with the python deep learning library of Keras (https://keras.io/). Also, at the time of starting this work, this model represented the good tradeoff between classification performance and huge parameters (Bianco et al., 2018).

The Inception-v3 architecture has 48 network layers with more than 23 million trainable weights. These layers are generally divided into feature extraction and classification parts. Weights of the feature extraction part are trained to describe common image characteristics such as curves, edges, gradients and particular patterns. These features are expected to be adopted to the task of ocean SAR vignette classification (Yosinski et al., 2014; Too et al., 2018; Wang et al., 2018a). The last layer of this CNN architecture represents the classification part, which is replaced with a new classification layer in our applications. Note that capability comparison of different CNN architectures may also be of interest, but it is beyond the scope of this work.

We examined two training strategies: transfer-learning and fine-tuning. The transfer-learning only trains the final classifier layer, while the fine-tuning adjusts all the layers in the CNN architec-

ture. For each input image, Inception-v3 requires the image size to be 299 pixels for both height and width. Then, 2048 optimal features per image are extracted to construct the final classifier. As noted above, the sensitivity of SAR to different oceanic or atmospheric phenomena can be different for the two WV incidence angles. We therefore create separate training datasets for WV1 and WV2 (hereafter TDwv1 and TDwv2). To equalize the size of TDwv1 and TDwv2, 320 images per class are randomly selected from the labelled dataset of TenGeoP-SARwv (Wang et al., 2018b). For training Inception-v3, the input dataset is randomly split into training and validation subsets with proportions of 70% and 30%. Training subset is fed into the CNN to learn and extract image features. The validation subset, by contrast, is used to gauge the CNN model performance at each epoch (iteration of CNN optimization).

3.2. CMwv model

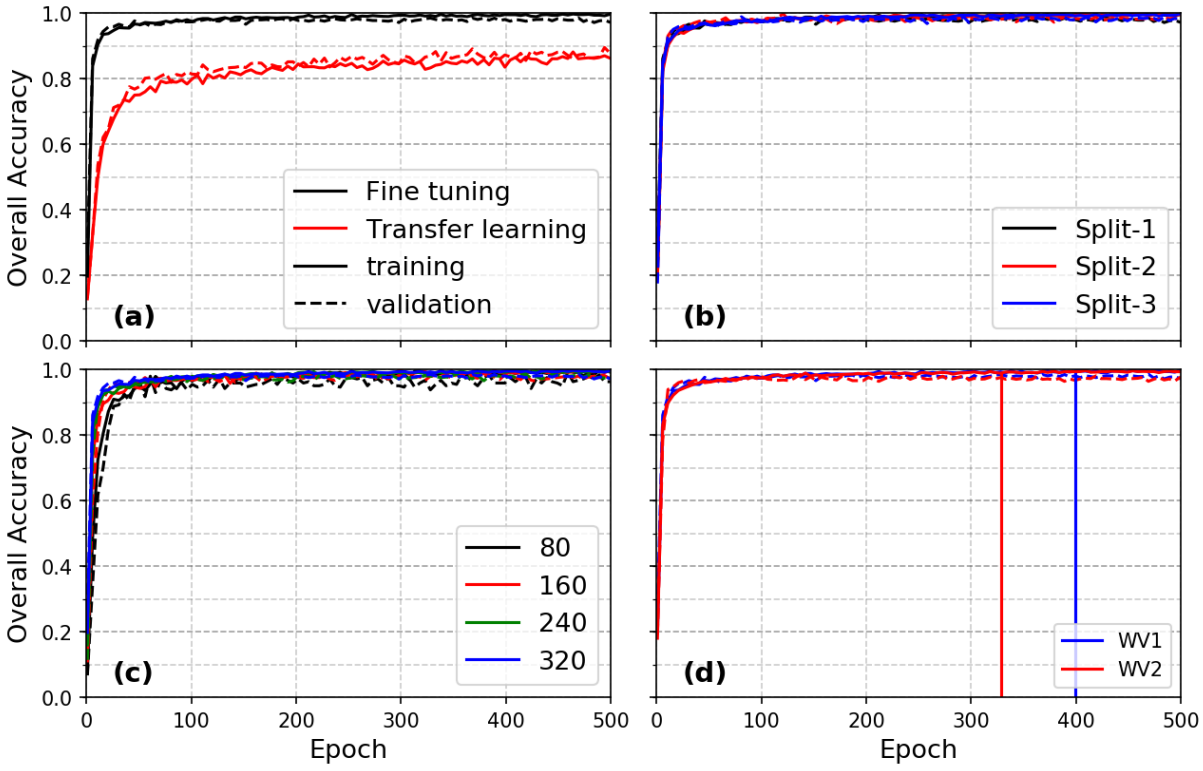

Figure 3: Overall accuracy (OA) in each 5 epochs during the training of inception-v3. The first 500 epochs are shown for (a) comparison of transfer-learning and fine-tuning, (b) experiment of random splitting process, (c) experiment of the training dataset size and (d) the development of CMwv.

First, we compare results found for the transfer-learning versus fine-tuning training approaches. Based on TDwv1, the Overall Accuracy (OA, Stehman (1997)) is calculated within 500 epochs

and is displayed in Figure 3 (a). As shown, the OA of both transfer-learning (red lines) and fine-tuning (black lines) increases rapidly within the first 100 epochs, and then remains stable at around 89% and 97%, respectively. Fine-tuning is more accurate than transfer-learning and is therefore chosen in this study. Figure 3 (b) displays the sensitivity assessment of the fine-tuning process to random training inputs. Random shuffling is repeated three times to generate different training and validation subsets drawn from TDwv1. Result shows no significant effect on OA due to different data draws. The impact of dataset size is also tested using image input datasets of 80, 160, 240 and 320 samples, respectively. All four models achieve comparable OA, as displayed in Figure 3 (c). The largest training dataset converges most quickly and with the highest and most constant OA. In this paper, we use 320 images per class to train the final model. Figure 3 (d) shows that OA improves rapidly with training epochs. The trained CNN weights at epochs 399 and 329 where OA reaches the maximum (blue and red vertical lines) are adopted in the final CMwv. This model has a OA of 98.5% and 98.3% for WV1 and WV2, respectively.

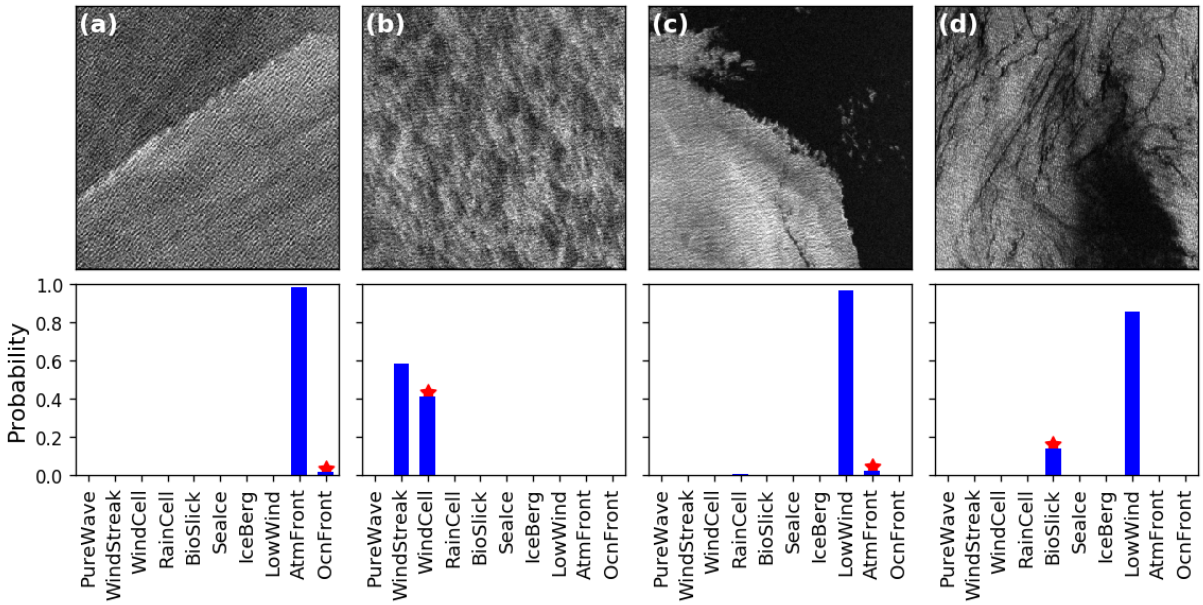

Figure 4: Examples of misclassified WV images from CMwv along with the classification probability of each class. Red stars indicate the class determined visually (manually-labelled).

Misclassifications still occur even though the model OA is very high. With visual inspection of the misclassified images in the validation part, four representative examples with their classification probabilities are shown in Figure 4. The red stars indicate the actual class. Ambiguous image features are one of the reasons leading to misclassification. For example in Figure 4 (a), the linear

feature of an oceanic front (OcnFront) looks more like the softer mottled linear features that we ascribed to the atmospheric front (AtmFront) class (Wang et al., 2019). Both cell-shaped features (WindCell) and the linear-shaped features (WindStreak) are visible in Figure 4 (b), also resulting in an ambiguity within this vignette. Superimposition of these two phenomena is captured by the CMwv model with high classification probabilities in both classes. Indeed, the atmospheric coherent structures that generate the WindStreak signature often undergo a transition to the convective structures that generate the WindCell signature when the surface buoyancy increases (Atkinson and Wu Zhang, 1996). Another reason responsible for misclassifications is that multiple geophysical phenomena can coexist within the same vignette. Low wind area (LowWind) is often associated with wind gust fronts (AtmFront), as shown in Figure 4 (c). Biological slicks (BioSlick) usually accompany the LowWind (Figure 4 (d)) because they both occur in low wind conditions. Signatures of ocean waves are also clearly seen in the four examples. The PureWave classification probability for these scenes is nearly zero due to our imposed lowest ranking of ocean waves within these prelabelled events. In other words, the priority of other phenomena in the developed classification model is much higher. This corresponds to the fact that our definition of PureWave is a SAR image that only contains signature of ocean waves without any other geophysical phenomena. It is thus expected that adjustment of our model to address multi-labelling with equal weights for these multiple feature SAR images might improve future classification. To this end, the current classification probabilities can be further exploited to get more fuzzy probabilities or refine the training dataset. A thorough labeling strategy allowing the existence of multiple features is also demanded. In particular, wave detection shall facilitate the labeling of its coexistence with other phenomena.

3.3. CMwv model assessment

To further assess the CMwv performance on the whole WV database, a quantitative figure was obtained through comparison against the independent assessment dataset introduced in Section 2.3. Figure 5 provides the normalized confusion matrix. The rows and columns in the matrix indicate the truth (manually-labelled) and CMwv prediction, respectively. One image is assigned to be the class of the largest classification probability. As shown, most of the class identification skill results for both WV1 and WV2 cases show accuracy that exceeds 0.8. One exception is PureWave, this class being strongly influenced by IceBerg, AtmFront and OcnFront events. This leads to much lower PureWave classification accuracy of 47% and 39% for WV1 and WV2, respectively. It is likely because signatures of ocean waves are prevalent in most images and we choose a loose

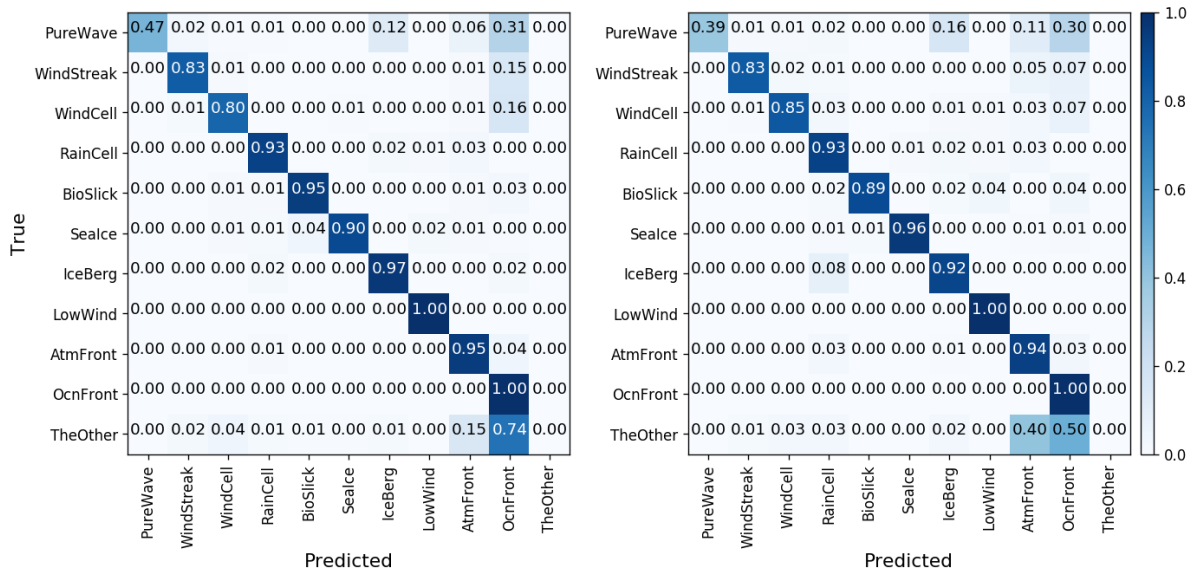

Figure 5: CMwv normalized confusion matrix when the model is applied to the WV1 (left) and WV2 (right) independent verification data subsets.

criteria for PureWave class in the assessment dataset. In addition, about 15% of WindStreak and WindCell images are misclassified as AtmFront and OcnFront, resulting in the relatively lower classification accuracy. Nearly 90% of the TheOther images are classified into categories of AtmFront and OcnFront. Overall, images of PureWave, IceBerg, AtmFront and OcnFront are often misclassified. To further quantify CMwv performance, recall, precision and F-score parameters (Sokolova and Lapalme, 2009) are calculated based on the confusion matrix:

$$Recall = \frac{number\ of\ correctly\ classified}{number\ of\ truth} \tag{1}$$

$$Precision = \frac{number\ of\ correctly\ classified}{number\ of\ classified} \tag{2}$$

$$F - score = \frac{2 \times precision \times recall}{precision + recall} \tag{3}$$

For given class, recall (also called sensitivity) is equivalent to the classification accuracy discussed above. Precision (also called positive predictability) indicates the model's internal accuracy or skill. The F-score takes both recall and precision into account as one comprehensive index for model performance. Values of these three parameters are all expected to be near one.

CMwv recall, precision and F-score results against the assessment dataset are given in Table 1. Results indicate a hierarchy in skill across classes where RainCell, BioSlick, SeaIce and

Table 1: CMwv recall, precision and F-score metrics for each of the 10 geophysical categories when applied to WV1 (upper) and WV2 (lower) vignette detection.

	PureWave	WindStreak	WindCell	RainCell	BioSlick	SeaIce	IceBerg	LowWind	AtmFront	OcnFront
Recall	0.47	0.83	0.80	0.93	0.95	0.90	0.97	1.00	0.95	1.00
	0.39	0.83	0.85	0.93	0.89	0.96	0.92	1.00	0.94	1.00
Precision	1.00	0.77	0.76	0.88	0.88	0.96	0.16	0.87	0.39	0.02
	0.98	0.96	0.94	0.80	0.91	0.96	0.18	0.79	0.38	0.02
F-score	0.64	0.80	0.78	0.90	0.91	0.93	0.27	0.93	0.56	0.04
	0.56	0.89	0.89	0.86	0.90	0.96	0.30	0.88	0.54	0.04

LowWind classes show similarly highest levels of recall, precision and F-scores that exceed 85% in any measure, and for both WV1 and WV2 vignettes. A second tier with slightly lower skill is seen for WindStreak and WindCell with WV2 F-scores of nearly 0.9 and 0.8 for WV2 and WV1 respectively. The drop in WV1 F-score is due to nearly 20% lower precision in WV1 scene detection. This is due to the fact that ocean wave signatures are suppressed at higher incidence and other atmospheric phenomena are more pronounced. Overall, the results indicate robust CMwv model performance for these six phenomena. A next drop in skill is seen for the PureWave class. PureWave detection shows much lower recall levels of 47% and 39% for WV1 and WV2, respectively. Inspection found that this is because a large number of PureWave dominated SAR scenes are misclassified as IceBerg (12% and 16%), AtmFront (6% and 11%), and OcnFront (31% and 30%), as shown in Figure 5. Yet, high PureWave precision suggests strong confidence when a PureWave detection occurs. The lowest performance tier is seen when CMwv is applied to detect icebergs, atmospheric, and ocean fronts (IceBerg, AtmFront and OcnFront). In these three classes, the model shows poor precision (i.e. an excess of false positives) caused by the misclassification of scenes that should have been ocean waves (PureWave) or more ambiguous events (TheOther).

Although time consuming, the visual classification provided by Wang et al. (2019) demonstrated the capabilities of S-1 WV to capture signatures of air-sea interactions. Above results suggest that an adapted deep CNN image recognition model can be trained for automated classification of the S-1 WV VV-polarized SAR vignettes. A brief summation of CMwv skill taken from these results suggests reasonable confidence levels for investigations that focus on six of the prescribed classes (WindStreak, WindCell, RainCell, BioSlick, SeaIce and LowWind), while CMwv refinements would be needed for OcnFront, AtmFront, IceBerg, and PureWave applications. Other deep learning techniques such as pixel-level based classification, object detection and image segmentation (Zhang et al., 2016; Cheng et al., 2017) are expected to efficiently target the

localized phenomena (RainCell, IceBerg, AtmFront and OcnFront) within each scene. In addition, it will be beneficial to include the geographic and time information of SAR data in deep learning approaches. Latitude is just one of many possible important and obvious data inputs, helping for example, to limit sea ice and iceberg detection windows to cold waters.

4. Geophysical applications

As a first demonstration, the CMwv model was applied to all S-1A WV VV-polarized acquisitions from March 2016 to February 2017. We examine the images classified as rain cells (RainCell) and sea ice (SeaIce) as well as their occurrence in space and time. GPM and IMERG rain precipitation and SSM/I sea ice concentration data are used for comparison. Specifically, seasonal variations of these two phenomena are presented and discussed in the four seasons: March-April-May (MAM), June-July-August (JJA), September-October-November (SON) and December-January-February (DJF) from March 2016 to February 2017. There are more than 160k vignettes acquired globally by S-1A in each of these seasons.

4.1. Rain cells

A detected RainCell in the S-1 vignettes has been defined as one or several km-scale circular- or semi-circular-shaped patches that may be either relatively bright or dark (Wang et al., 2019). These patches are typical signature of rain downdraft (Atlas, 1994; Alpers et al., 2016) in the convective rain cells (Houze, 1997). From March 2016 to February 2017, nearly 10% of S-1A images are classified as RainCell. The seasonal mapping of SAR-detected RainCell occurrence (fraction within 2° lat/lon bins) in the left panel of Figure 6 indicates distinct spatial and temporal patterns. We also plot the seasonal maps of monthly averaged IMERG rain rate in the right panel of Figure 6 for comparison. However, it must be noted here that the IMERG product aims at intercalibrating, merging, and interpolating satellite microwave precipitation estimates, together with microwave-calibrated infrared (IR) satellite estimates. This leads to different temporal and coverage resolution between SAR-detected RainCell occurrence and IMERG precipitation.

Across the whole tropical ocean (3 basins), SAR-detected rain events are found to be infrequent right along the equator with a band of strong occurrence north of the Equator. This band is clearly observed throughout the year and with the Inter-Tropical Convergence Zone (ITCZ). In the particular case of the Pacific ocean, strong occurrence of rain cells are also found in the South Pacific Convergence Zone. It is in good agreement with IMERG precipitation seasonal patterns. Significant differences are found in the subtropics between 10° and 30°. In the north hemisphere

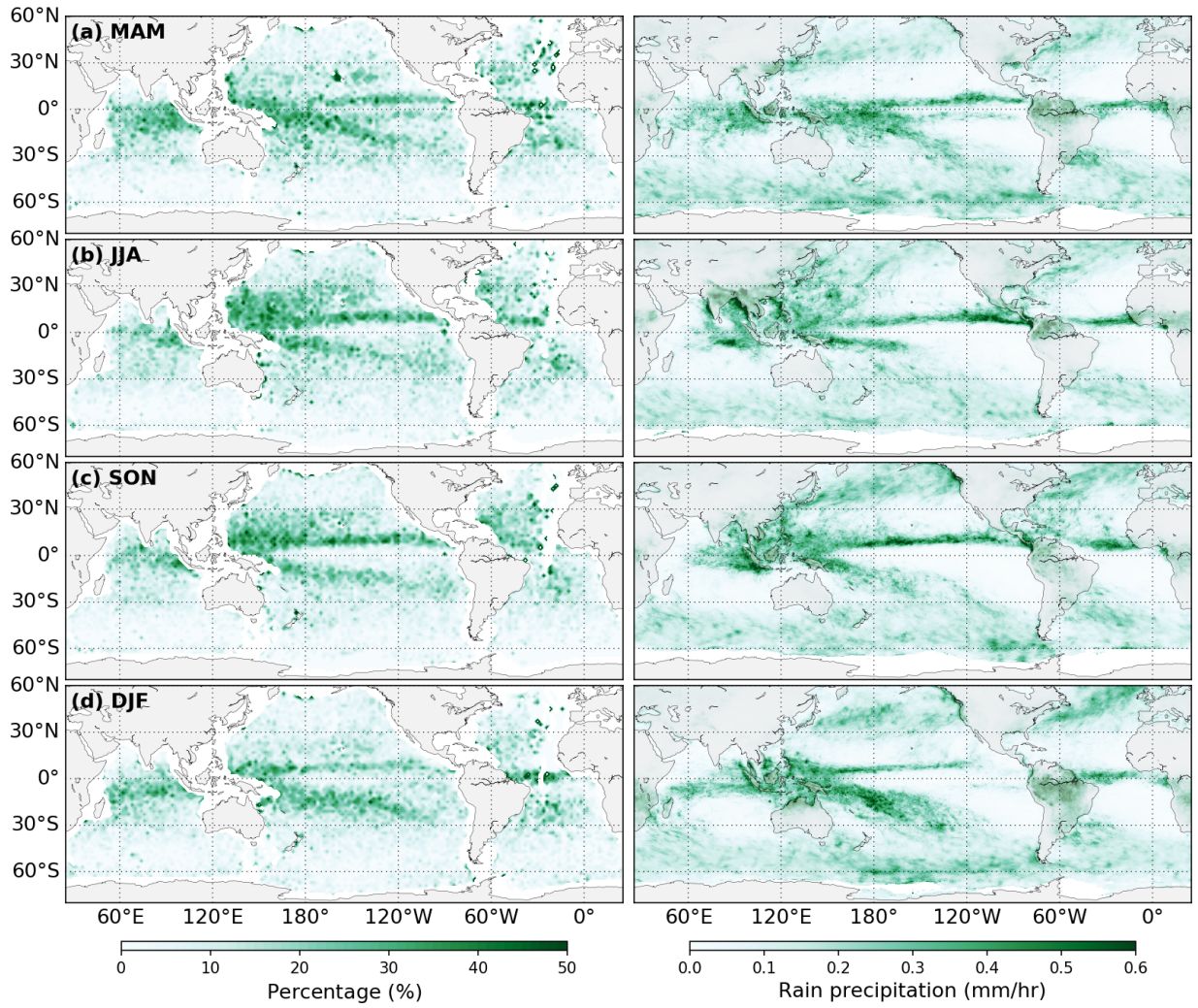

Figure 6: Seasonal comparison of CMwv-detected S-1A rain cells (left) alongside GPM precipitation measurements (right). Rain occurrence percentages are calculated on a 2° by 2° spatial grid based on S-1A WV data from March 2016 to February 2017. The average monthly rain rate in MAM, JJA, SON and DJF are obtained from the IMERG 0.1°-monthly product.

(Atlantic and Pacific), SAR-detected RainCell occurrence is high (>10%) whereas the rain precipitation from IMERG is low (<0.1 mm/hr). In the south hemisphere, this is also observed in the east of the south Pacific, in the Atlantic and in the Indian ocean. In the extratropical areas (poleward of 30°N or 30°S), we observe the opposite trend. SAR results present lower occurrence of RainCell while IMERG measures comparatively higher precipitation rates.

Overall, most areas of higher SAR-detected RainCell occurrence are associated with high IMERG precipitation areas and consistent with the rainfall climatology of previous studies (Kidd,

2001; Adler et al., 2003). However, disagreements are found as well. One of the reasons for this is due to the fact that IMEG products measure all types of rainfall and is not limited to rain cells. This certainly explains the agreement observed in the tropical area where the convective cells dominate (Houze, 1997). To further address the difference, a point-by-point collocation between S-1 WV SAR images and GPM level-2 DPR Ku-only surface rain precipitation is conducted. The collocation criteria is within 35 km in space and 10 min in time.

In total, there are 2588 matched data pairs with 286 SAR vignettes being classified as RainCell. For 63.4% of the RainCell-classified images, collocated GPM also reports precipitation. In the remaining cases, however, no precipitation is reported by GPM. Figure 7 (a1) and (a2) display two examples of this situation that SAR detects rain events while GPM does not. The upper panel shows the SAR images and the bottom gives the precipitation. The red dashed box, white box and white arrow indicate the collocated area, image box and surface wind vector, respectively. As shown, these two SAR images exhibit clear RainCell signatures, confirming the credibility of RainCell classification results. The precipitation is not resolved by GPM, possibly because they are short-lived and/or weak rain events. For the images that are not classified as RainCell, 23.2% of the collocated GPM reports precipitation. With the visual inspection, we confirmed that most of these images do not have clear RainCell signature as defined in Wang et al. (2019). Two such examples are shown in Figure 7 (b1) and (b2). RainCell signatures in SAR images are primarily caused by modulations of the surface waves due to rainfall, downdraft and also a direct attenuation of the signal by rain drops in the atmosphere (Alpers et al., 2016). However, we recall here that the first order impact on the sea surface roughness as detected by C-band active radar is the local wind. As a result, there is a competition between the ambient wind and possible rain impacts on the small-scale waves. Thus, we suspect that in situation where the wind speed is sufficiently high, the wind impact dominates the backscattering over the rain, yielding SAR scenes with hardly detectable rain signature. Figure 8 further evidences this interpretation. It is the distribution of surface wind speed for the four possible situations (SAR-detected RainCell or not, GPM DPR-measured precipitation or not). As shown, SAR-detected RainCell (blue and orange lines) occurs mostly at intermediate wind speed of 3-10 m/s. By contrast, the wind distribution of the images with non-detected RainCell but precipitation as given by GPM (red line) centers at 12 m/s. This implies that when the backscattering is mainly impacted by the high wind speed, the detectability of rain cell signatures weakens.

From these comparisons, we conclude that Deep Learning methods can be used to automatically identify SAR images impacted by rain cells. As a matter of fact, the high resolution of

SAR may complement the existing rainfall measurements available from space by detecting very short scale events. For now this potential seems limited to convective rain and is less relevant for high latitudes where sea state dominates the signature in SAR image, preventing for a reliable rain detection.

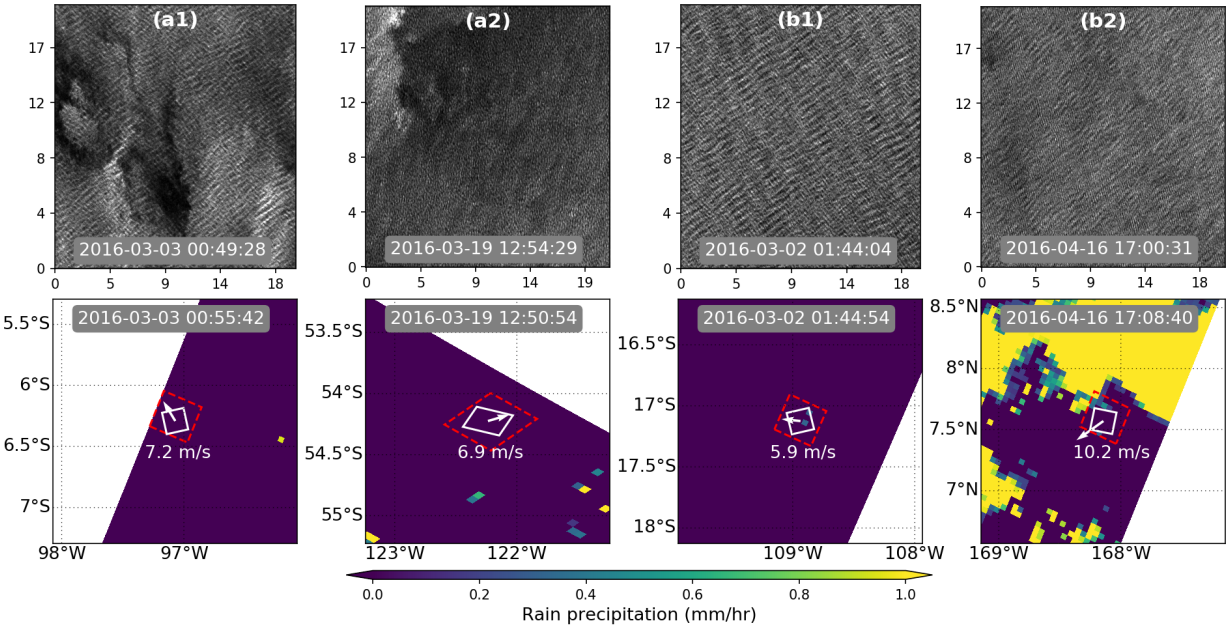

Figure 7: Four cases of point-by-point comparison between classified rain cells and the collocated GPM level-2 DPR Ku-only surface rain precipitation. (a1) and (a2) are cases in which WV detects RainCell and GPM indicates no precipitation. (b1) and (b2) are cases in which WV did not detect RainCell and GPM measured precipitation. Upper panels are WV images, lower panels show the GPM rain rate swath data. In the lower panels, the WV outline is the white box and the collocation region is the red box. The vector indicates the sea surface wind.

4.2. Sea Ice Near Antarctica

Interactions between sea ice, ocean, and the atmosphere in polar regions significantly impact global weather and climate systems (Fyke et al., 2018). Changing boundaries between the ocean and sea ice have dominant effects on marine ecosystem structure around the Antarctic (Tynan, 1998; Nicol et al., 2000). Monitoring of Southern Ocean sea ice has thus been of high interest among remote sensing and geoscience communities for many years. In this subsection, we assess sea ice (SeaIce) detected by CMwv near the Antarctica using S-1A WV SAR vignettes from March 2016 to February 2017. Note that our classification model distinguishes all type of SeaIce images from open ocean water.

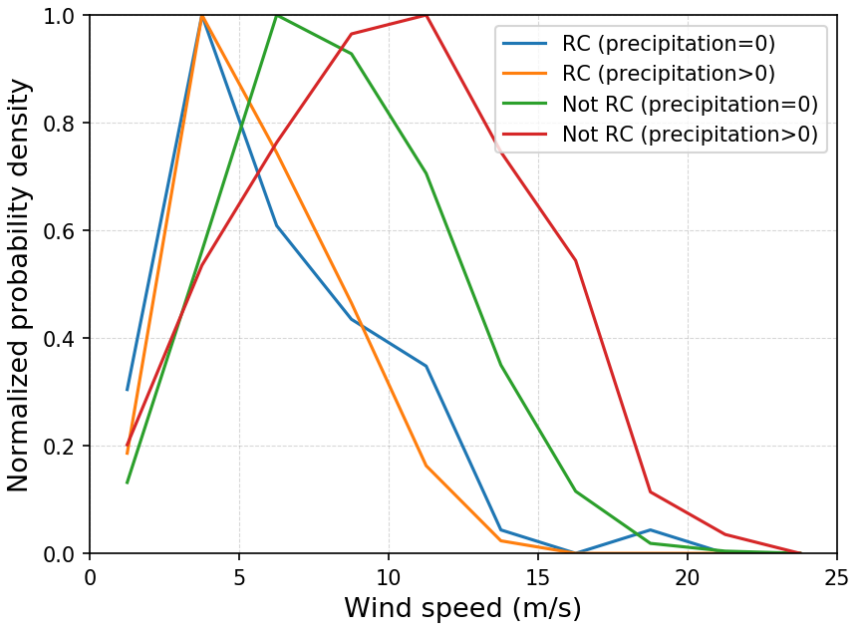

Figure 8: Normalized probability density function of surface wind speed for the point-by-point comparisons with condition of rain cells are detected or not and precipitation is measurable or not.

In total, there are nearly 25k vignettes classified as SeaIce. As shown in Figure 9 (a), most S-1A vignettes indicating SeaIce are distributed across the polar Southern Ocean. While the SeaIce subset mapping clearly shows a few misclassified cases of small islands, heavy rain and strong convection phenomena, the otherwise realistic geographic SeaIce distribution appears to confirm the high classification precision of 0.96 (see Table 1). Although the reason for misclassifications need further investigation, these misclassified SeaIce images can be easily filtered out according to the latitudes or SeaIce events occurrence map (see Figure 9 (c)). Figure 9 (b) provides the number of classified SeaIce SAR vignettes per month. As expected, the number of detected SeaIce vignettes has a clear seasonal variability, increasing from March to a maximum in October and subsequently decreasing. This variation is highly consistent with the seasonal cycle of Antarctic SeaIce extent (Doddridge and Marshall, 2017).

S-1A detected SeaIce occurrence is calculated on a 2 by 2 degree grid and shown in Figure 9 (c). It illustrates the seasonal variation view of SeaIce coverage around the Antarctica. The SeaIce extent is also denoted by the contour lines where occurrence percentage is equal to 10%. In the austral summer (DJF and MAM), most of the classified SeaIce lies close to the Antarctica and is poleward of 60°S. It is also clear that the SeaIce extent is non-uniformly distributed along the Antarctic coasts, with more SeaIce from 0°-60°W, and from 120°W-150°E. Varied SeaIce

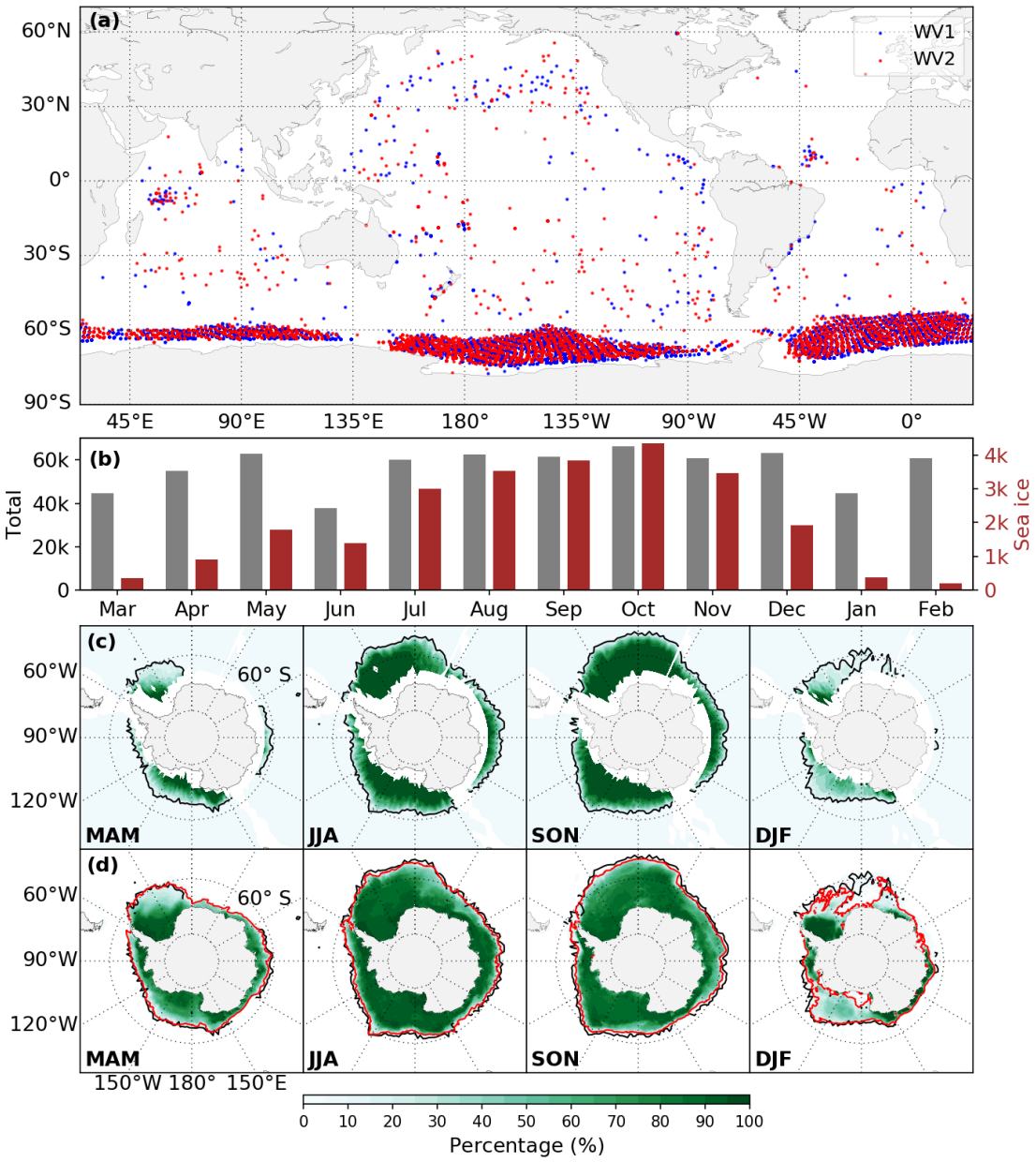

Figure 9: Ocean sea ice around the Antarctica from March 2016 to February 2017. (a) displays the locations of classified sea ice vignettes with blue and red colors indicating WV1 and WV2, respectively. (b) presents the total number of S-1A and sea ice detected vignettes for each month. Sea ice coverage in four seasons derived from the classified SAR vignettes are shown in (c) with color representing the occurrence percentage in 2° boxes. (d) shows the mean sea ice concentration from the SSM/I daily product. Contour lines in (c) and (d) are calculated from the occurrence percentage (black, 10%) and sea ice concentration (red, 10%), denoting the ice-water boundaries.

coverage also exists in the Antarctic winter from JJA to SON. As shown in Figure 9 (c), winter period SeaIce significantly expands in comparison to the austral summer. It even spreads north of 60°S between 10°E and 70°W during the summer. It is important to note that there is no WV SAR data acquired very close to the coast of or over Antarctica (Torres et al., 2012). This is the reason for the null/white space around the coastline in these maps. For comparison, seasonal maps of mean SeaIce concentration from the SSM/I daily product are provided in Figure 9 (d). Contour lines of SeaIce edge calculated from both the occurrence percentage (black) and SeaIce concentration (red) are superimposed on these maps. As shown, the patterns seen on the SAR-detected SeaIce largely mirrors these SeaIce concentration maps where both systems collect data. Boundaries between ocean water and SeaIce from SAR and SSM/I data are highly consistent with each other. This agreement is another measure of CMwv credibility as an WV data classification tool.

As demonstrated, these high-resolution WV acquisitions of SeaIce are another data catalogue to monitor SeaIce edge boundaries around the Antarctica. In particular, they can benefit the survey of wave-ice interactions. Indeed, a new method has been recently developed to derive the directional wave spectrum in the sea-ice, from which wave heights, periods and directions can be derived (Ardhuin et al., 2015). Stopa et al. (2018) used these extensive information to address the wave forces on sea ice through break-up and rafting, advancing the knowledge of wave-ice dynamics. With respect of the waves and sea ice interactions, the use of sea-ice classification in combination with waves-in-ice algorithm is certainly a perspective.

5. Conclusions

The S-1 WV SAR vignette classification model (CMwv) has been successfully developed by a SAR-adaptation of the Inception-v3 CNN image recognition architecture. Experimental testing of the training process indicates that fine-tuning is a more effective approach than transfer-learning. The CMwv mode is able to identify and assign detection probabilities to ten geophysical phenomena that are pre-defined in a hand-labelled dataset (TenGeoP-SARwv, Wang et al. (2018b)). To evaluate and quantify the performance of CMwv, recall, precision and F-scores are calculated against an independent assessment dataset. Results show that this classification tool works well for classes of WindStreak (wind streaks), WindCell (micro-convective cells), RainCell (rain cells), BioSlick (biological slicks), SeaIce (sea ice) and LowWind (low wind area). However, classification of PureWave (pure ocean waves) is limited with very high precision, but low recall. Class detections for IceBerg (icebergs), AtmFront (atmospheric fronts) and OcnFront (oceanic fronts)

are severely influenced by PureWave and the special category of TheOther. The developed classification model can directly be applied to S-1A&B WV datasets. In the near future, efforts to improve the classification of PureWave, IceBerg, AtmFront and OcnFront are necessary. In addition, the inclusion of new classes corresponding to other geophysical phenomena and the definition of a multi-labelled dataset would likely yield further improvements.

Two geophysical applications are demonstrated based on the classification results of S-1A WV vignettes from March 2016 to February 2017. Geophysical maps of classified rain cells and sea ice are qualitatively comparable to precipitation data from GPM and sea ice concentration from SSM/I. Results further verify the credibility of this classification tool. Moreover, once classified, access to the large catalogue of class-specific high-resolution WV vignettes may provide new and more detailed geophysical information to complement existing global ocean satellite measurements. The various geophysical phenomena captured within the massive S-1 A&B WV data suggest promise to further advance our understanding of air-sea interactions, particularly at sub-kilometer scales. Application of this CMwv tool to the growing three plus year of S-1 global ocean SAR data archive should allow, for the first time, access to the spatial (global and regional) and temporal (seasonal and inter-annual) statistics of numerous geophysical phenomena. This may, in turn, help to advance certain aspects of atmospheric and climate theory and numerical ocean and weather models.

This present work provides a basis to move application of ocean SAR remote sensing beyond the case study stage. It also demonstrates the potential of these global SAR WV mode vignettes for broader geophysical application, augmenting its operational role supporting ocean wave prediction systems. While this study is limited to the S-1 WV SAR acquisitions, the methodology could be applied to any other sub-scene (10-20 km) SAR data products from platforms such as ERS-1/2, Envisat/ASAR, TerraSAR-X, Gaofen-3 and CFOSAT. Similar exploitation of the full WV mode SAR data archive could provide a long-term (nearly 30 years) climatology including data on interannual and seasonal variability at global scale.

6. Acknowledgements

The authors are grateful to NASA, IFREMER and ECMWF for providing the rain, sea ice and wind data that are used in this study. We acknowledge the Sentinel-1 SAR data access via ESA and through Sentinel-1A Mission Performance Center (4000107360/12/I-LG). This study is also supported by S1-4SCI Ocean Study (4000115170/15/I-SBo), CNES TOSCA program (COWS project) and NASA Physical Oceanography grant (NNX17AH17G). C. Wang thanks to the finan-

cial support of China Scholarship Council (CSC) for his PhD. Additionally, we would like to thank the anonymous reviewers for their constructive comments concerning this manuscript.

References

Adler, R.F., Huffman, G.J., Chang, A., Ferraro, R., Xie, P.P., Janowiak, J., Rudolf, B., Schneider, U., Curtis, S., Bolvin, D., Gruber, A., Susskind, J., Arkin, P., Nelkin, E., 2003. The Version-2 Global Precipitation Climatology Project (GPCP) Monthly Precipitation Analysis (1979Present). Journal of Hydrometeorology doi:10.1175/1525-7541(2003)004<1147:TVGPCP>2.0.CO;2.

Alpers, W., Brümmer, B., 1994. Atmospheric boundary layer rolls observed by the synthetic aperture radar aboard the ERS-1 satellite. Journal of Geophysical Research: Oceans 99, 12613–12621. doi:10.1029/94JC00421.

Alpers, W., Huang, W., 2011. On the discrimination of radar signatures of atmospheric gravity waves and oceanic internal waves on synthetic aperture radar images of the sea surface. IEEE Transactions on Geoscience and Remote Sensing 49, 1114–1126. doi:10.1109/TGRS.2010.2072930.

Alpers, W., Zhang, B., Mouche, A., Zeng, K., Chan, P.W., 2016. Rain footprints on c-band synthetic aperture radar images of the ocean - revisited. Remote Sensing of Environment 187, 169–185. doi:10.1016/j.rse.2016.10.015.

Alpers, W.R., Ross, D.B., Rufenach, C.L., 1981. On the detectability of ocean surface waves by real and synthetic aperture radar. Journal of Geophysical Research: Oceans 86, 6481–6498. URL: http://dx.doi.org/10.1029/JC086iC07p06481, doi:10.1029/JC086iC07p06481.

Ardhuin, F., Collard, F., Chapron, B., Girard-Ardhuin, F., Guitton, G., Mouche, A., Stopa, J.E., 2015. Estimates of ocean wave heights and attenuation in sea ice using the sar wave mode on sentinel-1a. Geophysical Research Letters 42, 2317–2325. URL: https://agupubs.onlinelibrary.wiley.com/doi/abs/10.1002/2014GL062940, doi:10.1002/2014GL062940, arXiv:https://agupubs.onlinelibrary.wiley.com/doi/pdf/10.1002/2014GL062940.

Atkinson, B.W., Wu Zhang, J., 1996. Mesoscale shallow convection in the atmosphere. Reviews of Geophysics 34, 403. doi:10.1029/96RG02623.

Atlas, D., 1994. Origin of storm footprints on the sea seen by synthetic aperture radar. Science 266, 1364–1366. doi:10.1126/science.266.5189.1364.

Babin, S.M., Sikora, T.D., Winstead, N.S., 2003. A Case Study of Satellite Synthetic Aperture Radar Signatures of Spatially Evolving Atmospheric Convection over the Western Atlantic Ocean. Boundary-Layer Meteorology 106, 527–546. URL: https://doi.org/10.1023/A:1021236600569, doi:10.1023/A:1021236600569.

Bianco, S., Cadene, R., Celona, L., Napoletano, P., 2018. Benchmark analysis of representative deep neural network architectures. IEEE Access 6, 64270–64277. URL: https://doi.org/10.1109%2Faccess.2018.2877890, doi:10.1109/access.2018.2877890.

Carsey, F., Holt, B., 1987. Beaufort-Chukchi ice margin data from seasat: Ice motion. Journal of Geophysical Research: Oceans doi:10.1029/JC092iC07p07163.

Cheng, G., Han, J., 2016. A survey on object detection in optical remote sensing images. doi:10.1016/j.isprsjprs.2016.03.014, arXiv:1603.06201.

Cheng, G., Han, J., Lu, X., 2017. Remote Sensing Image Scene Classification: Benchmark and State of the Art. Proceedings of the IEEE 105, 1865–1883. doi:10.1109/JPROC.2017.2675998, arXiv:1703.00121.

Chunchuzov, I., Vachon, P.W., Li, X., 2000. Analysis and modeling of atmospheric gravity waves observed in RADARSAT SAR images. Remote Sensing of Environment 74, 343–361. doi:10.1016/S0034-4257(00)00076-6.

Collard, F., Ardhuin, F., Chapron, B., 2009. Monitoring and analysis of ocean swell fields from space: New methods for routine observations. Journal of Geophysical Research: Oceans doi:10.1029/2008JC005215.

Doddridge, E.W., Marshall, J., 2017. Modulation of the Seasonal Cycle of Antarctic Sea Ice Extent Related to the Southern Annular Mode. Geophysical Research Letters doi:10.1002/2017GL074319.

Ezraty, R., Girard-Ardhuin, F., Piolle, J.f., Kaleschke, L., Heygster, G., 2007. Arctic & Antarctic sea ice concentration and Arctic sea ice drift estimated from Special Sensor MIcrowave data - User's manual V2.1. URL: ftp://ftp.ifremer.fr/ifremer/cersat/products/gridded/psi-drift/documentation/ssmi.pdf.

Fu, L.L., Holt, B., 1982. Seasat views oceans and sea ice with synthetic-aperture radar. Technical Report. California Institute of Technology, Jet Propulsion Laboratory.

Fyke, J., Sergienko, O., Löfverström, M., Price, S., Lenaerts, J., 2018. An overview of interactions and feedbacks between ice sheets and the Earth system. Reviews of Geophysics URL: http://doi.wiley.com/10.1029/2018RG000600, doi:10.1029/2018RG000600.

Gerling T W, 1986. Structure of the surface wind field from the Seasat SAR. Journal of Geophysical Research doi:10.1029/JC091iC02p02308.

Hasselmann, K., Hasselmann, S., 1991. On the nonlinear mapping of an ocean wave spectrum into a synthetic aperture radar image spectrum and its inversion. Journal of Geophysical Research: Oceans 96, 10713–10729. URL: http://dx.doi.org/10.1029/91jc00302http://dx.doi.org/10.1029/91JC00302, doi:10.1029/91JC00302.

Hasselmann, K., Raney, R.K., Plant, W.J., Alpers, W., Shuchman, R.A., Lyzenga, D.R., Rufenach, C.L., Tucker, M.J., 1985. Theory of synthetic aperture radar ocean imaging: A MARSEN view. Journal of Geophysical Research: Oceans 90, 4659–4686. URL: http://dx.doi.org/10.1029/JC090iC03p04659, doi:10.1029/JC090iC03p04659.

Heimbach, P., Hasselmann, S., Hasselmann, K., 1998. Statistical analysis and intercomparison of WAM model data with global ERS-1 SAR wave mode spectral retrievals over 3 years. Journal of Geophysical Research doi:10.1029/97JC03203.

Hou, A.Y., Kakar, R.K., Neeck, S., Azarbarzin, A.A., Kummerow, C.D., Kojima, M., Oki, R., Nakamura, K., Iguchi, T., 2014. The global precipitation measurement mission. Bulletin of the American Meteorological Society doi:10.1175/BAMS-D-13-00164.1.

Houze, R.A., 1997. Stratiform Precipitation in Regions of Convection: A Meteorological Paradox? Bulletin of the American Meteorological Society doi:10.1175/1520-0477(1997)078<2179:SPIROC>2.0.CO;2, arXiv:arXiv:0801.1618v2.

Hu, F., Xia, G.S., Hu, J., Zhang, L., 2015. Transferring deep convolutional neural networks for the scene classification of high-resolution remote sensing imagery. Remote Sensing doi:10.3390/rs71114680.

Jackson, C.R., Apel, J.R., Editors, 2004. Synthetic Aperture Radar Marine User's Manual. US Department of Commerce, National Oceanic and Atmospheric Administration, National Environmental Satellite, Data, and Information Serve, Office of Research and Applications.

Jia, T., Liang, J.J., Li, X.M., Sha, J., 2018. SAR Observation and Numerical Simulation of Internal Solitary Wave Refraction and Reconnection Behind the Dongsha Atoll. Journal of Geophysical Research: Oceans doi:10.1002/2017JC013389.

Johannessen, J.a., Shuchman, R.a., Digranes, G., Lyzenga, D.R., Wackerman, C., Johannessen, O.M., Vachon, P.W., 1996. Coastal ocean fronts and eddies imaged with ERS 1 synthetic aperture radar. Journal of Geophysical Research 101, 6651. doi:10.1029/95JC02962.

Katsaros, K.B., Brown, R.A., 1991. Legacy of the Seasat Mission for Studies of the Atmosphere and Air-Sea-Ice Interactions. Bulletin of the American Meteorological Society doi:10.1175/1520-0477(1991)072<0967:LOTSMF>2.0.CO;2.

Kerbaol, V., Chapron, B., Vachon, P.W., 1998. Analysis of ERS-1/2 synthetic aperture radar wave mode imagettes. Journal of Geophysical Research: Oceans 103, 7833–7846. URL: http://dx.doi.org/10.1029/97JC01579, doi:10.1029/97JC01579.

Kidd, C., 2001. Satellite rainfall climatology: A review. International Journal of Climatology doi:10.1002/joc.635.

LeCun, Y., Bengio, Y., Hinton, G., 2015. Deep learning. Nature 521, 436–444. URL: http://www.nature.com/doifinder/10.1038/nature14539, doi:10.1038/nature14539, arXiv:arXiv:1312.6184v5.

Lehner, S., Schulz-Stellenfleth, J., Schättler, B., Breit, H.H., Horstmann, J., 2000. Wind and Wave Measurements Using Complex ERS-2 SAR Wave Mode Data. IEEE Transactions on Geoscience and Remote Sensing 38, 2246–2257. doi:10.1109/TGRS.2003.814658.

Levy, G., 2001. Boundary layer roll statistics from SAR. Geophysical Research Letters 28, 1993–1995. URL: http://doi.wiley.com/10.1029/2000GL012667, doi:10.1029/2000GL012667.

Li, W., Wu, G., Zhang, F., Du, Q., 2017. Hyperspectral Image Classification Using Deep Pixel-Pair Features. IEEE Transactions on Geoscience and Remote Sensing doi:10.1109/TGRS.2016.2616355.

Li, X., Zheng, W., Pichel, W.G., Zou, C.Z., Clemente-Col??n, P., 2007. Coastal katabatic winds imaged by SAR. Geophysical Research Letters 34. doi:10.1029/2006GL028055.

Li, X., Zheng, W., Yang, X., Zhang, J.A., Pichel, W.G., Li, Z., 2013. Coexistence of Atmospheric Gravity Waves and Boundary Layer Rolls Observed by SAR*. Journal of the Atmospheric Sciences 70, 3448–3459. URL: http://dx.doi.org/10.1175/JAS-D-12-0347.1, doi:10.1175/JAS-D-12-0347.1.

Meadows, G.A., Shuchman, R.A., Tseng, Y.C., Kasischke, E.S., 1983. Seasat synthetic aperture radar observations of wave-current and wave-topographic interactions. Journal of Geophysical Research doi:10.1029/JC088iC07p04393.

Mouche, A.A., Collard, F., Chapron, B., Dagestad, K.F., Guitton, G., Johannessen, J.A., Kerbaol, V., Hansen, M.W., 2012. On the Use of Doppler Shift for Sea Surface Wind Retrieval From SAR. IEEE Transactions on Geoscience and Remote Sensing 50, 2901–2909. doi:10.1109/TGRS.2011.2174998.

Nicol, S., Pauly, T., Bindoff, N.L., Wright, S., Thiele, D., Hosle, G.W., Strutton, P.G., Woehler, E., 2000. Ocean circulation off east Antarctica affects ecosystem structure and sea-ice extent. Nature doi:10.1038/35020053.

Rascle, N., Molemaker, J., Marié, L., Nouguier, F., Chapron, B., Lund, B., Mouche, A., 2017. Intense deformation field at oceanic front inferred from directional sea surface roughness observations. Geophysical Research Letters 44, 5599–5608. doi:10.1002/2017GL073473.

Russakovsky, O., Deng, J., Su, H., Krause, J., Satheesh, S., Ma, S., Huang, Z., Karpathy, A., Khosla, A., Bernstein, M., Berg, A.C., Fei-Fei, L., 2015. ImageNet Large Scale Visual Recognition Challenge. International Journal of

Computer Vision doi:10.1007/s11263-015-0816-y, arXiv:1409.0575.

Sikora, T.D., Young, G.S., Fisher, C.M., Stepp, M.D., 2011. A synthetic aperture radar-based climatology of open-cell convection over the northeast Pacific Ocean. Journal of Applied Meteorology and Climatology 50, 594–603. doi:10.1175/2010JAMC2624.1.

Sokolova, M., Lapalme, G., 2009. A systematic analysis of performance measures for classification tasks. Information Processing and Management 45, 427–437. doi:10.1016/j.ipm.2009.03.002.

Stehman, S.V., 1997. Selecting and interpreting measures of thematic classification accuracy. Remote Sensing of Environment doi:10.1016/S0034-4257(97)00083-7.

Stopa, J.E., Ardhuin, F., Husson, R., Jiang, H., Chapron, B., Collard, F., 2016. Swell dissipation from 10 years of Envisat advanced synthetic aperture radar in wave mode. Geophysical Research Letters doi:10.1002/2015GL067566.

Stopa, J.E., Mouche, A., 2017. Significant wave heights from Sentinel-1 SAR: Validation and applications. Journal of Geophysical Research: Oceans 122, 1827–1848. URL: http://dx.doi.org/10.1002/2016JC012364, doi:10.1002/2016JC012364.

Stopa, J.E., Sutherland, P., Ardhuin, F., 2018. Strong and highly variable push of ocean waves on Southern Ocean sea ice. Proceedings of the National Academy of Sciences doi:10.1073/pnas.1802011115.

Szegedy, C., Liu, W., Jia, Y., Sermanet, P., Reed, S., Anguelov, D., Erhan, D., Vanhoucke, V., Rabinovich, A., 2015. Going deeper with convolutions, in: Proceedings of the IEEE Computer Society Conference on Computer Vision and Pattern Recognition, pp. 1–9. doi:10.1109/CVPR.2015.7298594, arXiv:1409.4842.

Szegedy, C., Vanhoucke, V., Ioffe, S., Shlens, J., Wojna, Z., 2016. Rethinking the inception architecture for computer vision, in: 2016 IEEE Conference on Computer Vision and Pattern Recognition (CVPR), pp. 2818–2826. doi:10.1109/CVPR.2016.308.

Too, E.C., Yujian, L., Njuki, S., Yingchun, L., 2018. A comparative study of fine-tuning deep learning models for plant disease identification. doi:10.1016/j.compag.2018.03.032.

Topouzelis, K., Kitsiou, D., 2015. Detection and classification of mesoscale atmospheric phenomena above sea in SAR imagery. Remote Sensing of Environment 160, 263–272. doi:10.1016/j.rse.2015.02.006.

Torres, R., Snoeij, P., Geudtner, D., Bibby, D., Davidson, M., Attema, E., Potin, P., Rommen, B.r., Floury, N., Brown, M., Traver, I.N., Deghaye, P., Duesmann, B., Rosich, B., Miranda, N., Bruno, C., L'Abbate, M., Croci, R., Pietropaolo, A., Huchler, M., Rostan, F., 2012. GMES Sentinel-1 mission. Remote Sensing of Environment 120, 9–24. URL: http://www.sciencedirect.com/science/article/pii/S0034425712000600, doi:10.1016/j.rse.2011.05.028.

Tynan, C.T., 1998. Ecological importance of the Southern Boundary of the Antarctic Circumpolar Current. Nature doi:10.1038/33675, arXiv:0402594v3.

Wang, C., Mouche, A., Tandeo, P., Stopa, J., Chapron, B., Foster, R., Vandemark, D., 2018a. Automated Geophysical Classification of Sentinel-1 Wave Mode SAR Images Through Deep-Learning, in: IGARSS 2018 - 2018 IEEE International Geoscience and Remote Sensing Symposium, IEEE. pp. 1776–1779. URL: https://ieeexplore.ieee.org/document/8518354/, doi:10.1109/IGARSS.2018.8518354.

Wang, C., Mouche, A., Tandeo, P., Stopa, J., Longépé, N., Erhard, G., Foster, R., Vandemark, D., Chapron, B., 2018b. Labeled SAR imagery dataset of ten geophysical phenomena from Sentinel-1 wave mode (TenGeoP-SARwv). doi:10.17882/56796.

Wang, C., Mouche, A., Tandeo, P., Stopa, J.E., Longépé, N., Erhard, G., Foster, R.C., Vandemark, D., Chapron, B., 2019. A labelled ocean SAR imagery dataset of ten geophysical phenomena from Sentinel1 wave mode. Geoscience Data Journal 0, gdj3.73. URL: https://onlinelibrary.wiley.com/doi/abs/10.1002/gdj3.73, doi:10.1002/gdj3.73.

Winstead, N.S., Colle, B., Bond, N., Young, G., Olson, J., Loescher, K., Monaldo, F., Thompson, D., Pichel, W., 2006. Using sar remote sensing, field observations, and models to better understand coastal flows in the gulf of alaska. Bulletin of the American Meteorological Society doi:10.1175/BAMS-87-6-787.

Yosinski, J., Clune, J., Bengio, Y., Lipson, H., 2014. How transferable are features in deep neural networks?, in: Ghahramani, Z., Welling, M., Cortes, C., Lawrence, N.D., Weinberger, K.Q. (Eds.), Advances in Neural Information Processing Systems 27. Curran Associates, Inc., pp. 3320–3328.

Young, G.S., Sikora, T.N., Winstead, N.S., 2005. Use of Synthetic Aperture Radar in Finescale Surface Analysis of Synoptic-Scale Fronts at Sea. Weather and Forecasting 20, 311–327. doi:10.1175/WAF853.1.

Zhang, L., Zhang, L., Du, B., 2016. Deep learning for remote sensing data: A technical tutorial on the state of the art. IEEE Geoscience and Remote Sensing Magazine 4, 22–40. doi:10.1109/MGRS.2016.2540798.

Zhao, W., Du, S., 2016. Spectral-Spatial Feature Extraction for Hyperspectral Image Classification: A Dimension Reduction and Deep Learning Approach. IEEE Transactions on Geoscience and Remote Sensing doi:10.1109/TGRS.2016.2543748.

Zhao, Y., Li, X.M., Sha, J., 2016. Sea surface wind streaks in spaceborne synthetic aperture radar imagery. Journal of Geophysical Research: Oceans 121, 6731–6741. URL: http://dx.doi.org/10.1002/2016JC012040, doi:10.1002/2016JC012040.

Zhou, W., Newsam, S., Li, C., Shao, Z., 2017. Learning low dimensional convolutional neural networks for high-resolution remote sensing image retrieval. Remote Sensing doi:10.3390/rs9050489.

Zhu, X.X., Tuia, D., Mou, L., Xia, G.S., Zhang, L., Xu, F., Fraundorfer, F., 2017. Deep Learning in Remote Sensing: A Comprehensive Review and List of Resources. doi:10.1109/MGRS.2017.2762307, arXiv:1710.03959.

List of Figure Captions

- Figure 1: Global distribution of the WV SAR data obtained by S-1A in July of 2016. Color is indicative of the SAR image density in 2° by 2° spatial grid.

- Figure 2: Ten vignette examples of expertly-defined geophysical phenomena. From (a) to (j) are pure ocean waves (PureWave), wind streaks (WindStreak), micro convective cells (WindCell), rain cells (RainCell), biological slicks (BioSlick), sea ice (SeaIce), icebergs (IceBerg), low wind area (LowWind), atmospheric front (AtmFront) and oceanic front (OcnFront).

- Figure 3: Overall accuracy (OA) in each 5 epochs during the training of inception-v3. The first 500 epochs are shown for (a) comparison of transfer-learning and fine-tuning, (b) ex-

periment of random splitting process, (c) experiment of the training dataset size and (d) the development of CMwv.

- Figure 4: Examples of misclassified WV images from CMwv along with the classification probability of each class. Red stars indicate the class determined visually (manually-labelled).

- Figure 5: CMwv normalized confusion matrix when the model is applied to the WV1 (left) and WV2 (right) independent verification data subsets.

- Figure 6: Seasonal comparison of CMwv-detected S-1A rain cells (left) alongside GPM precipitation measurements (right). Rain occurrence percentages are calculated on a 2° by 2° spatial grid based on S-1A WV data from March 2016 to February 2017. The average monthly rain rate in MAM, JJA, SON and DJF are obtained from the IMERG 0.1°-monthly product.

- Figure 7: Four cases of point-by-point comparison between classified rain cells and the collocated GPM level-2 DPR Ku-only surface rain precipitation. (a1) and (a2) are cases in which WV detects RainCell and GPM indicates no precipitation. (b1) and (b2) are cases in which WV did not detect RainCell and GPM measured precipitation. Upper panels are WV images, lower panels show the GPM rain rate swath data. In the lower panels, the WV outline is the white box and the collocation region is the red box. The vector indicates the sea surface wind.

- Figure 8: Normalized probability density function of surface wind speed for the point-by-point comparisons with condition of rain cells are detected or not and precipitation is measurable or not.

- Figure 9: Ocean sea ice around the Antarctica from March 2016 to February 2017. (a) displays the locations of classified sea ice vignettes with blue and red colors indicating WV1 and WV2, respectively. (b) presents the total number of S-1A and sea ice detected vignettes for each month. Sea ice coverage in four seasons derived from the classified SAR vignettes are shown in (c) with color representing the occurrence percentage in 2° boxes. (d) shows the mean sea ice concentration from the SSM/I daily product. Contour lines in (c) and (d) are calculated from the occurrence percentage (black, 10%) and sea ice concentration (red, 10%), denoting the ice-water boundaries.